Link to publication

University of Bath

Delay of Stall by Small Amplitude Airfoil Oscillations at Low Reynolds Numbers

D. J. Cleaver[1], Z. Wang[2] and I. Gursul[3]
University of Bath, Bath, BA2 7AY, UK

Particle Image Velocimetry and force measurements were conducted for small amplitude plunging motion of a NACA0012 airfoil at a post-stall angle of attack. Time-averaged flow shows that the region of separation is significantly reduced compared to a stationary airfoil. At low Strouhal numbers phase-averaged flow shows the formation and convection of leading-edge vortices, followed by their destructive interaction with the trailing-edge vortices. This mode of vortex flow is modified substantially at a critical Strouhal number. In this new mode, the leading-edge vortex is generated during the downward motion of the airfoil, but dissipates rapidly during the upward motion of the airfoil. Hence the convection of the leading-edge vortices is not observed. The strong interaction between the airfoil and vortex appears to destroy the coherency of the vortex. The switch between modes occurs at lower Strouhal numbers with increasing plunge amplitude. The critical Strouhal number corresponds to a Strouhal number based on the peak-to-peak amplitude $Sr_A = 0.25 - 0.42$. The point of drag to thrust switch correlates strongly with the point of mode-switch.

Nomenclature

a	=	amplitude of plunging motion
C_d	=	time-averaged drag coefficient
C_{d0}	=	drag coefficient of stationary airfoil
c	=	chord length
f	=	frequency of oscillation
$h(t)$	=	plunging displacement of the airfoil
Re	=	Reynolds number, $\rho U_\infty c / \mu$
Sr_A	=	Strouhal number based on peak-to-peak amplitude, $2fa/U_\infty$
Sr_c	=	Strouhal number based on chord length, fc/U_∞
t	=	time
T	=	plunge period
U_∞	=	free stream velocity
V	=	magnitude of velocity vector
x	=	streamwise direction
y	=	cross-stream direction
α	=	angle of attack
μ	=	viscosity
ρ	=	density
ω	=	vorticity

I. Introduction

There is currently growing interest in the field of Micro Air Vehicles (MAVs) due to their potential for a wide variety of military and civil applications. A MAV is classically defined as a vehicle with major dimension less than 15 cm. At this scale the small Reynolds numbers encountered make lift and thrust creation a challenge due to dominant viscous effects.

---

[1] Postgraduate Student, Dept. of Mechanical Engineering, AIAA Student Member.
[2] RCUK Academic Fellow, Dept. of Mechanical Engineering.
[3] Professor, Dept. of Mechanical Engineering, Associate Fellow AIAA.

One possible solution inspired by nature is flapping flight. The aerodynamic feats achieved by birds and insects demonstrate its true potential. For example[1], a barn swallow can achieve roll rates of $5000°s^{-1}$, compared to an A4 Skyhawk's $720°s^{-1}$, and an insect can land upside-down whilst most aircraft require a specially prepared 2-mile landing strip. These feats are achieved through unsteady aerodynamic phenomena (eg. Leading Edge Vortex (LEV), clap-and-fling, wing-wake interference) that are unexplainable through steady-state theory. Producing these phenomena requires very complex wing-kinematics consisting of flexing, twisting, bending, rotating or feathering during the flapping cycle[2], in conjunction with complex and very responsive control systems. It is therefore unlikely that man will be able to replicate nature's abilities in the foreseeable future.

A more immediate solution could be to improve the aerodynamic performance of fixed wing MAVs and develop capabilities for improved maneuverability. Given the low Reynolds numbers, active or passive flow control will be necessary to increase lift and delay stall. However, conventional flow control techniques such as blowing are not practical at these small scales and often there is not enough space for them. The principal objective of this research is therefore to exploit fluid-structure interactions to control separated flows, increase lift and delay stall. We present preliminary evidence of lift enhancement and stall delay on airfoils oscillating with small-amplitude and high frequency. Such flow control and lift enhancement could be useful for cruise flight as well as gust encounters.

The idea of flow control with forced (small-amplitude) wing oscillations has been demonstrated for nonslender delta wings by our group[3]. More interestingly, self-excited wing vibrations of a flexible delta wing can lead to impressive lift enhancement[4]. Similarly, self-excited membrane vibrations can cause a delay in stall for membrane wings as demonstrated numerically[5] and experimentally[6]. Our focus in this work is on lift enhancement and stall delay for two-dimensional rigid airfoils oscillating with small amplitude. For a two-dimensional airfoil the reattachment process is fundamentally different from that of a delta wing. The dominant feature of a delta wing is a strong leading-edge vortex, where spanwise removal of vorticity is beneficial in flow reattachment. For two-dimensional airfoils (large aspect ratio wings), this mechanism is absent.

Detailed in this paper are experiments conducted at the University of Bath studying the flow field and drag characteristics of a NACA0012 undergoing a sinusoidal plunging motion with small amplitude (a/c=0.025 to 0.200). Both Particle Image Velocimetry (PIV) and force measurements have been performed. Although both drag and lift force measurements were taken, only the drag measurements shall be presented here. The lift force measurements along with further PIV data shall be presented in a future paper.

II.   Experimental Apparatus and Procedures

Force measurements and PIV experiments were conducted on a plunging NACA0012 mounted vertically in a closed-loop water tunnel. The experimental parameters and their ranges are shown in Table 1; uncertainties are calculated based on the methods of Moffat[7]. Force uncertainties were calculated for all data points taking into account both bias and precision errors. For convenience only typical examples are shown in Table 1.

Table 1 Experimental Parameters

Variable	Range Considered	Range Presented	Uncertainty
Re	10,000 to 30,000	10,000	+/- 200
α	0° to 20°	15°	+/- 0.5°
a/c	0.025 to 0.200	0.025 to 0.200	+/- 0.003
Sr_c	0 to 3	0 to 3	+/- 2.33%
C_d/C_{d0}	1 to -5	1 to -5	+/- 0.16

A. Experimental Setup

The experiments were conducted in a free-surface closed-loop water tunnel (Eidetics Model 1520) at the University of Bath. The water tunnel is capable of flow speeds in the range 0-0.5 m/s and has a working section of dimensions 381 mm x 508 mm x 1530 mm. The turbulence intensity has previously been measured[8] to be less than 0.5%.

A NACA0012 airfoil of dimensions 0.1 m chord x 0.3 m span was mounted vertically in a 'shaker' mechanism, as shown in Fig. 1. The airfoil was constructed by selective laser sintering from Duraform Polyamide. It was placed between upper and lower end plates, with clearances maintained at 2 mm. Velocity, flow visualization and force measurements showed static stall to commence at $\alpha = 10°$. At $\alpha = 15°$ the airfoil is therefore fully stalled. This is in agreement with previous studies at comparable Reynolds numbers[9-13].

The oscillations were supplied via a Motavario 0.37kW three-phase motor, 5:1 wormgear and IMO Jaguar Controller. The position of the root of the airfoil was measured through a rotary encoder fixed to the spindle of the worm gear shaft. The rotary encoder was also used to trigger the PIV system.

B. Force Measurements

The forces applied in both the streamwise and cross-stream directions were measured via a two-component aluminium binocular strain gauge force balance[14], however only those in the streamwise direction are presented here. One of the major deficiencies of this design is that to function, a strain must be produced, thereby introducing flexibility. Due to inertia forces being dominant and proportional to the square of frequency the forces experienced at $Sr_c = 3$ were approximately nine times the forces at $Sr_c = 1$. A force balance designed for use at $Sr_c = 1$ would therefore produce excessively large trailing edge displacements at $Sr_c = 3$ (as the airfoil is supported in a similar manner to a cantilevered beam); and one designed for $Sr_c = 3$ would be inaccurate at $Sr_c = 1$. Three force balances were therefore used of varying rigidities. Data was taken across the entire range for all three force balances so as to validate each other. Generally the agreement between the three different force balances was extremely good.

The signal from the strain gauges was amplified by a Wheatstone bridge circuit and sampled at either 2 kHz for 20,000 samples (static cases), or 360 per cycle for a minimum of 50 cycles (dynamic cases). Each data point was taken three times for each force balance and the forces calculated from the average voltage through the linear calibration curves. To minimize uncertainties these calibration curves consisted of twenty three points and were performed daily before and after testing.

C. PIV Measurements

A TSI 2D-PIV system was used to measure the velocity field in the vicinity of the airfoil. For measurements over the upper surface of the airfoil, the laser was positioned behind as shown in Fig. 1. The shadow created by the airfoil therefore obscured the lower surface. For measurements over the lower surface the laser was positioned near the side wall of the tunnel. In both cases, the camera was located under the tunnel as shown in Fig. 1. The PIV images were analyzed using the software Insight 3G. A recursive FFT correlator was selected to generate a vector field of 199x148 vectors for the upper surface (~1.22 mm spatial resolution) and 399x297 for the lower surface (~0.27 mm spatial resolution). The time-averaged data is derived from 500 pairs of images, the phase-averaged from 100 pairs for the upper surface and 250 pairs for the lower surface. For the phase-averaged data a total of either 4, 8 or 24 sets were taken at regular intervals throughout the cycle.

III.   Results

A. Time-Averaged Flow Field

Figure 2a presents the streamlines and the magnitude of the velocity vector for a stationary NACA0012 airfoil at an angle of attack of $\alpha = 15^\circ$. It is seen that, as expected, there is a large region of separation over the suction surface of the airfoil. Therefore the airfoil can be classified as fully stalled which is in agreement with force measurements, flow visualization and previous studies[9-13].

Figure 2b demonstrates that the region of separation is significantly reduced through oscillation even at low frequencies ($Sr_c = 0.50$) and small amplitudes (a/c = 0.025). It is worth noting that due to the nature of time-averaged measurements the region in the direct vicinity of the airfoil surface is masked by the motion, i.e. the maximum displacement of the airfoil (shown as dotted airfoil) limits the possible measurement domain. The region of separation therefore appears smaller than is necessarily true. Taking this into account the region of separation is still clearly reduced. A second interesting feature is a region of higher velocity above the leading edge. As will be shown later, this coincides with the region of formation of a leading edge vortex (LEV). With increasing frequency (Figures 2c to g), the reduction in the region of separation and increased velocity at the leading edge continue.

At a Strouhal number of $Sr_c = 2.0$ (Fig. 2e) a region of low velocity is observed above the trailing edge, while there is also a small region of high velocity downstream of the trailing-edge. As shown later this coincides with the development of counter-clockwise trailing edge vortices (TEVs) which remain near the trailing edge during their formation. The phase-averaged vorticity data also shows a reverse von Kármán vortex street forming at the trailing edge. This coincides with the small jet observed in the time-averaged data. These four flow features (reduced separation region, high velocity near the leading edge, low velocity above the trailing edge, and a small time-averaged jet at the trailing-edge) continue to develop with increasing Strouhal number.

At an increased amplitude of a/c = 0.05 similar flow features are observed but with greater effect for the same Strouhal number, as shown in Fig. 3. The region of separation is significantly reduced so that for Strouhal numbers above 2.0 there is no discernible separation over the upper surface. The high velocity region above the leading edge

is observed for all Strouhal numbers. It grows in size and magnitude for Strouhal numbers up to $Sr_c = 2$, then becoming smaller and more concentrated beyond this. The reduction of the separation region with increasing frequency implies a reduction in drag and increase in lift as the separation is delayed in the time-averaged sense.

The development of a trailing-edge jet is shown through the high velocity region observed at Strouhal numbers of 1.5, 2.0, 2.5 and 3.0. At larger Strouhal numbers the high velocity jet begins to dominate. For $Sr_c = 3.0$, this jet has a maximum velocity three times greater than the freestream as measured half a chord length downstream of the trailing edge. The phase-averaged vorticity data shows the cause of this jet to be a reverse von Kármán vortex street.

B. Phase-Averaged Flow Field

Figure 4 shows the phase-averaged normalized vorticity at two points in the cycle (at the maximum and minimum plunging displacement) for various Strouhal numbers and $a/c = 0.05$. At the lowest Strouhal number ($Sr_c = 1.0$), multiple distinct clockwise vortices form at the leading edge per cycle (Fig. 4a). This is clearer in the movie of the vorticity field. Whereas the weaker vortices dissipate rapidly, the strongest one convects along the upper surface and is then ingested into the wake through destructive interaction with the counter-clockwise trailing edge vortices. At the trailing edge three counter-clockwise vortices are formed and shed per cycle.

As the Strouhal number is increased to $Sr_c = 1.5$ (Fig. 4b), the multiple LEVs shed per cycle become a single LEV of greater maximum negative vorticity. There is also a weaker vortex with opposite sign created by the vortex/boundary interaction. At the trailing edge a single counter-clockwise vortex and two weaker clockwise vortices are shed per cycle. The LEV is shed and interacts destructively with the counter-clockwise trailing edge vortex. The creation of the large TEV and its interaction with the large LEV results in the rapid dissipation of the LEV.

As the Strouhal number is increased to $Sr_c = 2.0$ (Fig. 4c), the leading-edge vortex and the secondary vortex of opposite sign become stronger. The strength of the counter-clockwise TEVs increases significantly as there are now clockwise vortices generated at the trailing-edge. Every second clockwise TEV merges with the clockwise LEV. A particularly interesting feature at this Strouhal number is that two pairs of trailing edge vortices are shed per cycle creating two 'branches' in the wake. This wake bears a strong resemblance to the neutral wakes of Lai and Platzer[15] that are created during the transition from drag to thrust.

At $Sr_c = 2.5$ (Fig. 4d) the flow field has changed significantly. The LEV remains close to the leading edge for longer in the cycle and once convected is significantly weaker. The interaction of the LEV, secondary vortex, and the oscillating airfoil result in rapid dissipation of the LEV. The weak LEV convects along the surface, but its effect on the wake is minimal. It is interesting to note the position of the shed LEV over the airfoil at the same point in the oscillation cycle for different Strouhal numbers. At the maximum displacement (left column) of the airfoil, for $Sr_c = 1.0$ it is approximately at $x/c = 0.5$, for $Sr_c = 1.5$ at $x/c = 0.35$, for $Sr_c = 2.0$ at $x/c = 0.25$, for $Sr_c = 2.5$ at $x/c = 0.1$, and for $Sr_c = 3$ the LEV is not visible. This implies that a minimum time is required for the formation and shedding of the LEV independent of the frequency or plunge velocity. At the trailing-edge for $Sr_c = 2.5$ stronger clockwise vortices are generated in addition to the very strong single vortex of counter-clockwise rotation. These two vortices form a single strong pair demonstrating a clear reverse von Kármán vortex street approximately aligned with the chord-line of the airfoil.

Further increase in Strouhal number to $Sr_c = 3.0$ (Fig. 4e) causes the LEV to remain entirely attached, i.e. there is no noticeable convection of the LEV. Even though the LEV is generated (as seen close to the leading-edge at the minimum displacement of the airfoil), it is dissipated quickly, and there is no convection of any vorticity concentration along the suction surface. The TEVs are larger and stronger which is in good agreement with the strong jet observed in the time-averaged data (Fig. 3g).

Figure 5 shows eight phase averaged vorticity plots throughout the cycle for the same case ($Sr_c = 3.0$) as in Figures 3g and 4e. It demonstrates that the LEV is formed late in the downward motion (Figures 5d and 5e) so that it is strongest at the bottom of the motion (Fig. 5e). During the upward motion the LEV appears to be sucked around the leading edge of the airfoil in a similar manner to the mode-1 of Lu et al.[16]. As the distance between the LEV and the airfoil is small, the details of the interaction during the upward motion are difficult to resolve. This interaction will be discussed for a larger plunge amplitude later in the paper.

As would be expected the downward motion of the trailing edge creates the counter-clockwise TEV whereas the upward motion creates the slightly smaller, weaker, clockwise TEV. These two vortices become paired and convect downstream along a path approximately parallel to the chordline of the airfoil. Figure 6 shows that these TEVs induce large velocities, the maximum being over six times the freestream. In addition, Fig. 6 demonstrates that the large region of separation witnessed for a stationary NACA0012 (Fig. 3a) is eradicated for almost the entire oscillation cycle. The only region of separation observed is at the maximum displacement (Fig. 6a) and relatively

small, from $x/c = 0.7$ to the trailing edge. This low velocity region coincides with the region of formation of a clockwise TEV.

During the downward motion (Figures 6b to 6e) the streamlines curve around the forming LEV and downwards into the airfoil. The streamlines therefore imply the flow is into the airfoil however it is important to note that the airfoil is in motion. Likewise during the upward motion (Figures 6f to 6a) the streamlines curve upwards out of the airfoil. The formation of an LEV is noticeable in all phases except (a). Given the strong LEV, lack of separation, and strong reverse von Kármán vortex street, one would anticipate significant improvements in both lift and drag performance.

To investigate the details of the interaction of the LEV with the airfoil, PIV measurements were taken for a larger amplitude ($a/c = 0.10$) over both upper and lower surfaces for $Sr_c = 0.75$. In Fig. 7, the upper surface demonstrates the same behavior as for the previous cases; an LEV forms during the downward motion (Figures 7a to 7e), and is not convected despite being a reasonable distance from the airfoil (see Fig. 7e), but instead appears to be sucked around the leading edge (Figures g to h). The lower surface measurements show however that this is not the case. Indeed the only negative vorticity observed over the lower surface is that created at the stagnation point during the formation of the LEV (Fig. 7c). It is therefore concluded that the LEV is not sucked around the leading edge but destroyed through impingement with the upward moving airfoil.

Henceforth flow fields of this nature, i.e. those demonstrating an attached LEV and no convection along the surface, shall be termed a mode-2 flow field. Those with a distinguishable shed and convected LEV (e.g. Fig. 4b) shall be termed a mode-1. Intermediate flow fields i.e. those with a weak convected LEV like Fig. 4d, shall be termed mixed. Based on these definitions one can compare the occurrence of the different flow fields for a wide variety of amplitudes thereby producing Fig. 8. This demonstrates that the switch from mode-1 to mode-2 depends upon both amplitude and frequency. The dashed line shows the approximate boundary, based on observations of the flow field. Although decreasing Strouhal number for increasing amplitude appears to suggest a constant plunge velocity for the switch between the modes, as discussed below this is a very approximate relationship.

C. Drag Force

Figure 9 shows the time-averaged drag force for various amplitudes normalized with respect to the value for the stationary airfoil. The most immediately apparent feature is the well documented switch from drag to thrust production that occurs for all amplitudes except $a/c = 0.025$. As expected the position of this switch is dependent on both frequency and amplitude, with the drag-to-thrust (D-T) switch occurring at lower frequencies for higher amplitudes.

Garrick approximations would suggest that the D-T switch should occur at an approximately constant plunge velocity for small amplitudes[17], however when the drag force data are plotted against Sr_A, the switch occurs in the range $Sr_A = 0.25 - 0.42$ (Fig. 10). It is therefore concluded that at non-zero angles of attack plunge velocity is not a good measure of drag characteristics. The assumptions made in Garrick-based approximations break down due to large regions of separation. The point of D-T switch does however bear a strong correlation with the point of mode-switch, as shown in Fig. 8. It is suggested that the mode-2 attached LEV may facilitate thrust production through two possible mechanisms: i) it allows clockwise vorticity shed from the trailing-edge to form the clockwise vortex at the trailing edge, ii) it does not destructively interact with the counter-clockwise TEV.

IV. Conclusions

PIV and force measurements show that small amplitude oscillations of a NACA0012 airfoil can significantly improve performance. At low Strouhal numbers the region of separation is significantly reduced in a time-averaged sense. Phase-averaged measurements show leading edge vortices form, and are convected into the wake where they interact destructively with vortices shed from the trailing edge. This was termed a mode-1 flow field. Generation of leading-edge vortices and their convection along the upper surface increase the momentum transfer between the free stream and separation region. This delays the flow separation and also brings the shear layer closer to the airfoil surface. These features are similar to the recent results of simulations[18] for a cambered airfoil plunging with small amplitude.

With increasing Strouhal number, the multiple LEVs form into a single LEV that is shed later and later in the cycle. At a critical Strouhal number, the LEV convection is not seen, and only an attached LEV is noticeable, this was termed a mode-2 flow field. The mode-2 LEV is generated during the downward motion of the airfoil, but dissipates rapidly during the upward motion of the airfoil. This strong interaction between the airfoil and vortex, which appears to destroy the coherency of the vortex, was documented at different plunge amplitudes. The switch between modes was found to occur at lower Strouhal numbers for higher plunge amplitudes. The critical Strouhal

number corresponds to a Strouhal number based on the peak-to-peak amplitude: Sr_A=0.25 - 0.42. The mode-2 LEV allows stronger clockwise TEVs to form and furthermore the LEV does not interact destructively with the counter-clockwise TEVs. As a result, mode-2 flow fields exhibit strong reverse von Kármán vortex streets and the jet associated with them. Indeed the point of drag-to-thrust switch correlates strongly with the point of mode-switch.

Acknowledgments

References

[1]Shyy, W., Berg, M., and Ljungqvist, D., "Flapping and Flexible Wings for Biological and Micro Air Vehicles" *Progress in Aerospace Sciences*, Vol. 35, No. 5, 1999, pp. 455-505.

[2]Ho, S., Nassef, H., Pornsinsirirak, N., Tai, Y.C., and Ho, C.M. "Unsteady Aerodynamics and Flow Control for Flapping Wing Flyers" *Progress in Aerospace Sciences*, Vol. 39, No. 8, 2003, pp. 635-681.

[3]Vardaki, E., Wang, Z., and Gursul, I., "Flow Reattachment and Vortex Re-formation on Oscillating Low Aspect Ratio Wings" *AIAA Journal*, Vol. 46, No. 6, June 2008, pp. 1453-1462.

[4]Taylor, G., Wang, Z., Vardaki, E., and Gursul, I., "Lift Enhancement over Flexible Nonslender Delta Wings" *AIAA Journal*, vol. 45, no. 12, December 2007, pp. 2979-2993.

[5]Gordnier, R., "High Fidelity Computational Simulation of a Membrane Wing Airfoil" *46th AIAA Aerospace Sciences Meeting and Exhibit*, AIAA-2008-614, 7-10 January, 2008, Reno, Nevada.

[6]Rojratsirikul, P., Wang, Z., and Gursul, I., "Unsteady Aerodynamics of Membrane Airfoils" (invited) *46th AIAA Aerospace Sciences Meeting and Exhibit*, AIAA-2008-0613, 7-10 January 2008, Reno, Nevada.

[7]Moffat, R.J. "Contributions to the Theory of Single-Sample Uncertainty Analysis" *Journal of Fluids Engineering-Transactions of the ASME*, Vol. 104, No. 2, 1982, pp. 250-260.

[8]Heathcote, S., "Flexible Flapping Airfoil Propulsion at Low Reynolds Numbers" Ph.D. Dissertation, Dept of Mechanical Engineering, University of Bath, Bath, UK, 2006.

[9]Shyy, W., Klevebring, F., Nilsson, M., Sloan, J., Carroll, B., and Fuentes, C., "Rigid and Flexible Low Reynolds Number Airfoils" *Journal of Aircraft*, Vol. 36, No. 3, 1999, pp. 523-529.

[10]Maresca, C., Favier, D., and Rebont, J., "Experiments on an Aerofoil at High Angle of Incidence in Longitudinal Oscillations" *Journal of Fluid Mechanics*, Vol. 92, No. Jun, 1979, pp. 671-690.

[11]Chen, J.M., and Choa, C.C., "Freestream Disturbance Effects on an Airfoil Pitching at Constant Rate" *Journal of Aircraft*, Vol. 36, No. 3, 1999, pp. 507-514.

[12]Laitone, E.V., "Aerodynamic Lift at Reynolds Numbers Below 7 x 10(4)" *AIAA Journal*, Vol. 34, No. 9, 1996, pp. 1941-1942.

[13]Sunada, S., Yasuda, T., Yasuda, K., and Kawachi, K., "Comparison of Wing Characteristics at an Ultralow Reynolds Number" *Journal of Aircraft*, Vol. 39, No. 2, 2002, pp. 331-338.

[14]Frampton, K.D., Goldfarb, M., Monopoli, D., and Cveticanin, D., "Passive aeroelastic tailoring for optimal flapping wings" *Proceedings of Conference on Fixed, Flapping and Rotary Wing Vehicles at Very Low Reynolds Numbers*, Notre Dame, USA, 2000, pp. 473-482.

[15]Lai, J.C.S., and Platzer, M.F., "Jet Characteristics of a Plunging Airfoil" *AIAA Journal*, Vol. 37, No. 12, 1999, pp. 1529-1537.

[16]Lu, X.Y., Yang, J.M., and Yin, X.Z., "Propulsive Performance and Vortex Shedding of a Foil in Flapping Flight" *Acta Mechanica*, Vol. 165, No. 3-4, 2003, pp. 189-206.

[17]Young, J., and Lai, J.C.S., "Oscillation Frequency and Amplitude Effects on the Wake of a Plunging Airfoil" *AIAA Journal*, Vol. 42, No. 10, 2004, pp. 2042-2052.

[18]Visbal, M., "High-Fidelity Simulation of Transitional Flow Past Plunging Airfoils" *47th AIAA Aerospace Sciences Meeting*, AIAA-2009-391, Orlando, Florida, 2009.
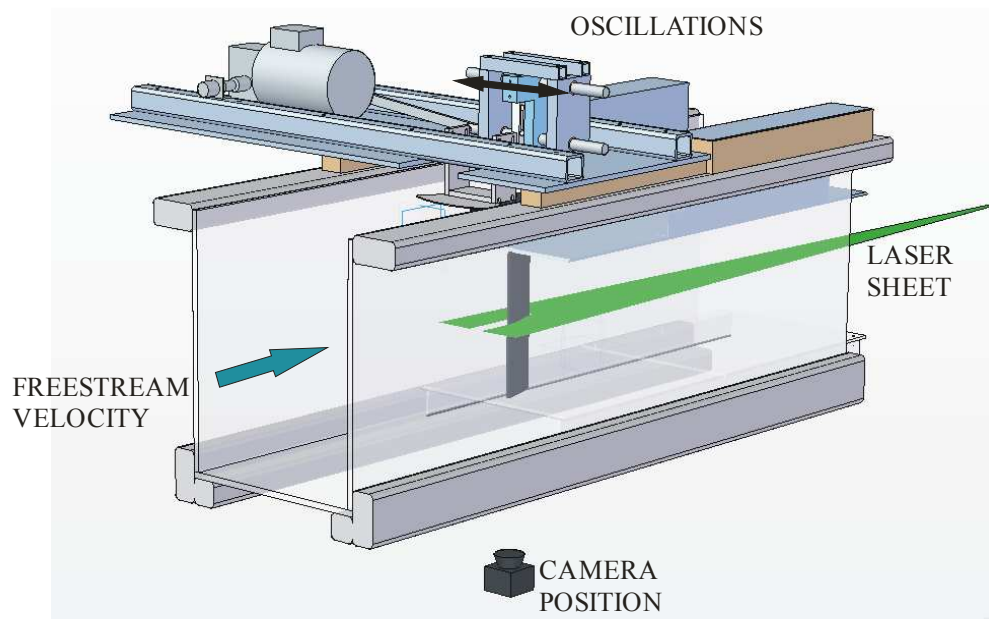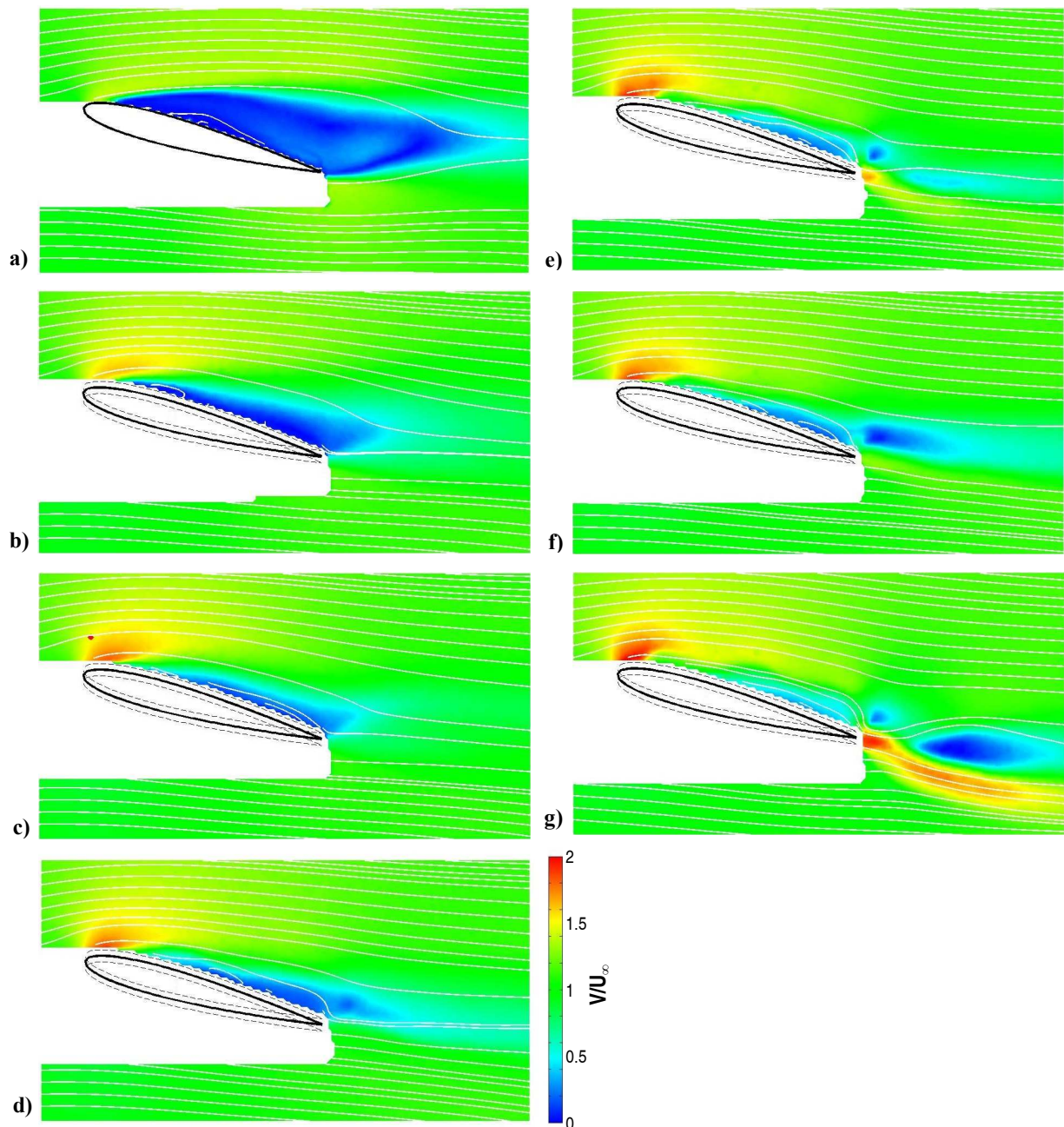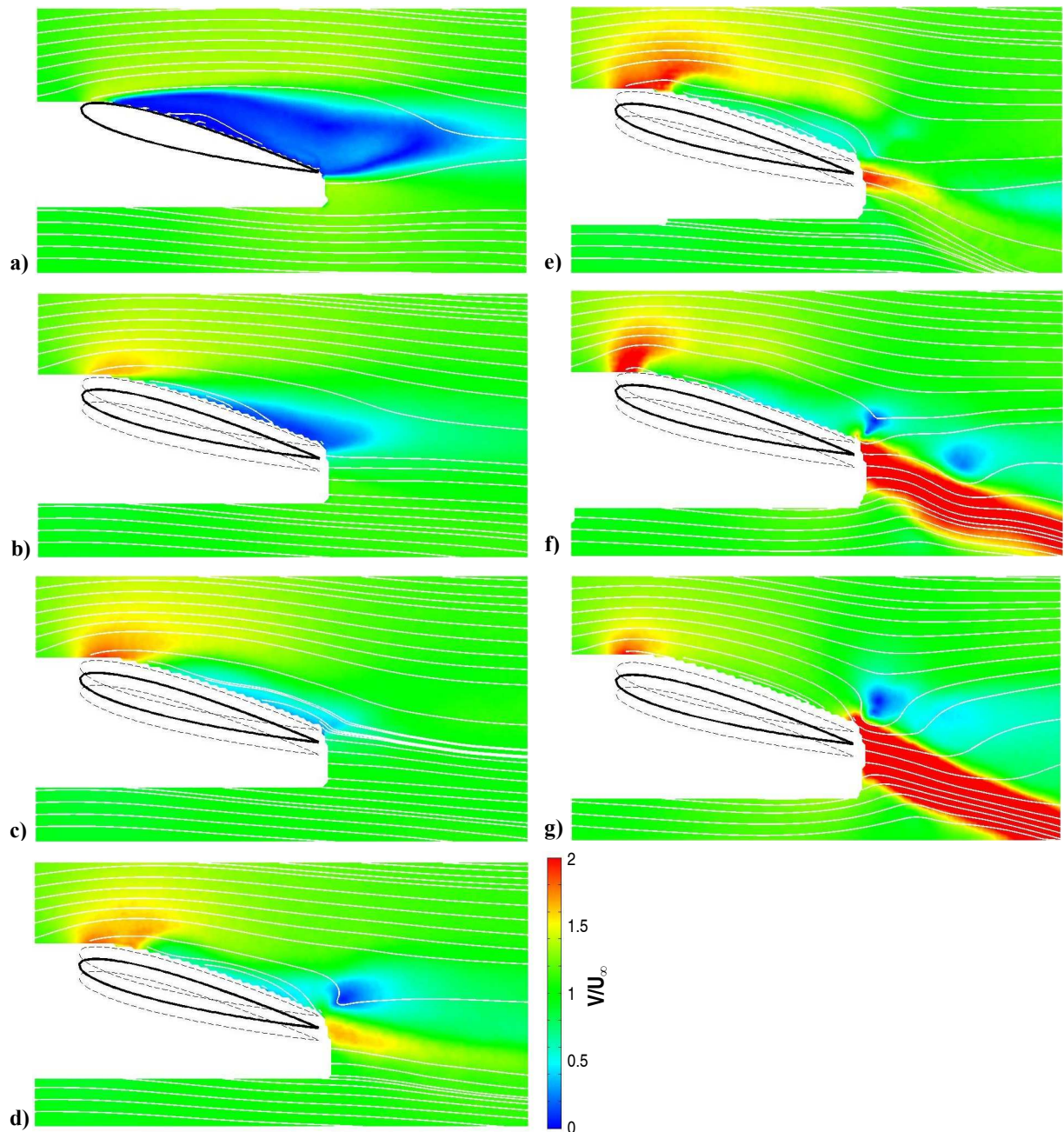
Figure 1. Experimental Setup.

Figure 2. Magnitude of time-averaged velocity for a/c = 0.025: a) stationary; b) Sr_c = 0.5; c) Sr_c = 1.0; d) Sr_c = 1.5; e) Sr_c = 2.0; f) Sr_c = 2.5 and g) Sr_c = 3.0.
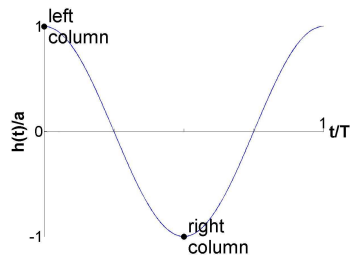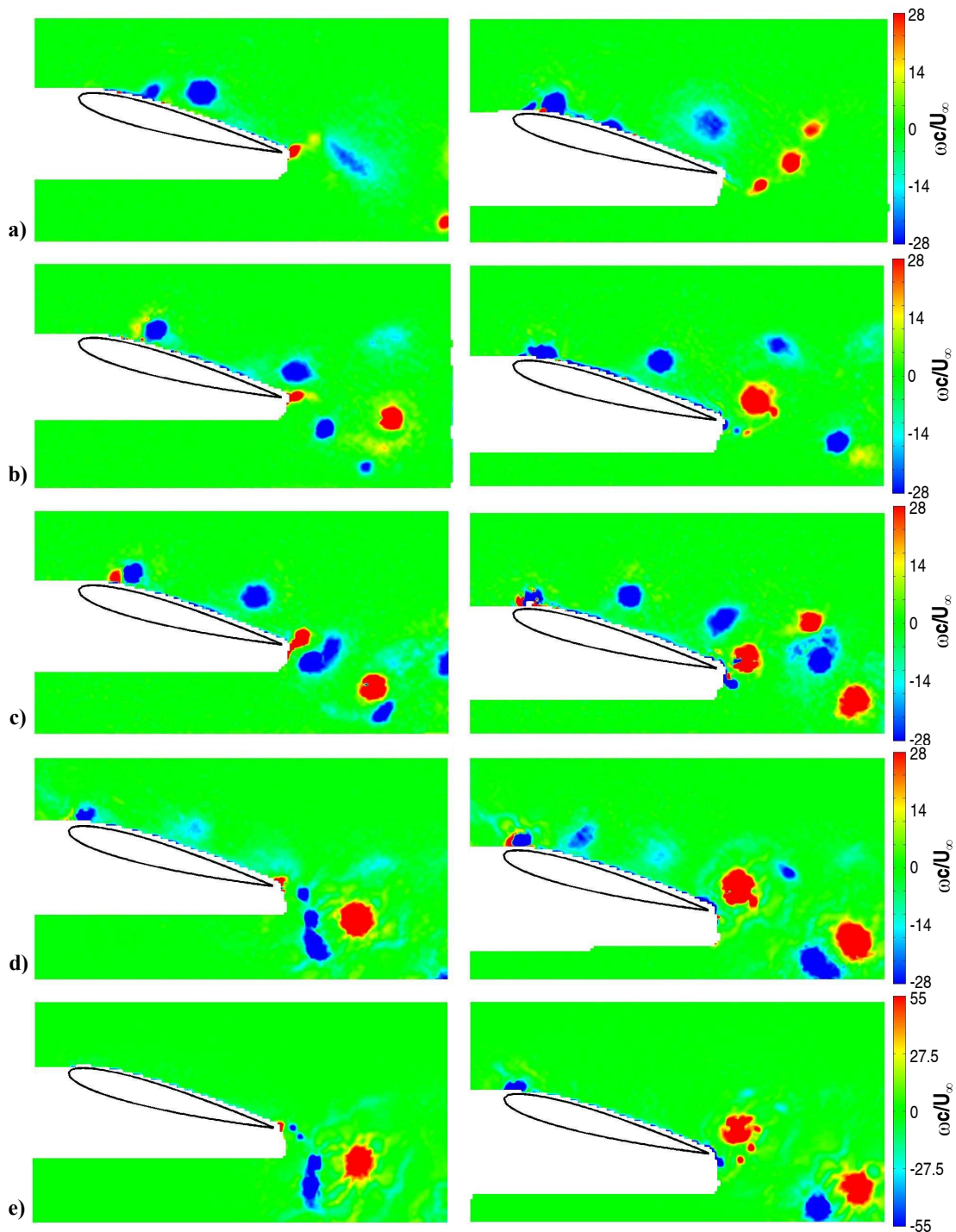
American Institute of Aeronautics and Astronautics

Figure 3. Magnitude of time-averaged velocity for a/c = 0.050: a) stationary; b) Sr$_c$ = 0.5; c) Sr$_c$ = 1.0; d) Sr$_c$ = 1.5; e) Sr$_c$ = 2.0; f) Sr$_c$ = 2.5 and g) Sr$_c$ = 3.0.

Figure 4. Phase-averaged vorticity, $\omega c/U_\infty$, at maximum (left) and minimum (right) of airfoil displacement for $a/c = 0.050$: a) $Sr_c = 1.0$; b) $Sr_c = 1.5$; c) $Sr_c = 2.0$; d) $Sr_c = 2.5$; e) $Sr_c = 3.0$. a) through c) demonstrate mode-1, e) demonstrates mode-2, and d) demonstrates a mixed mode. Note the different scale of e).
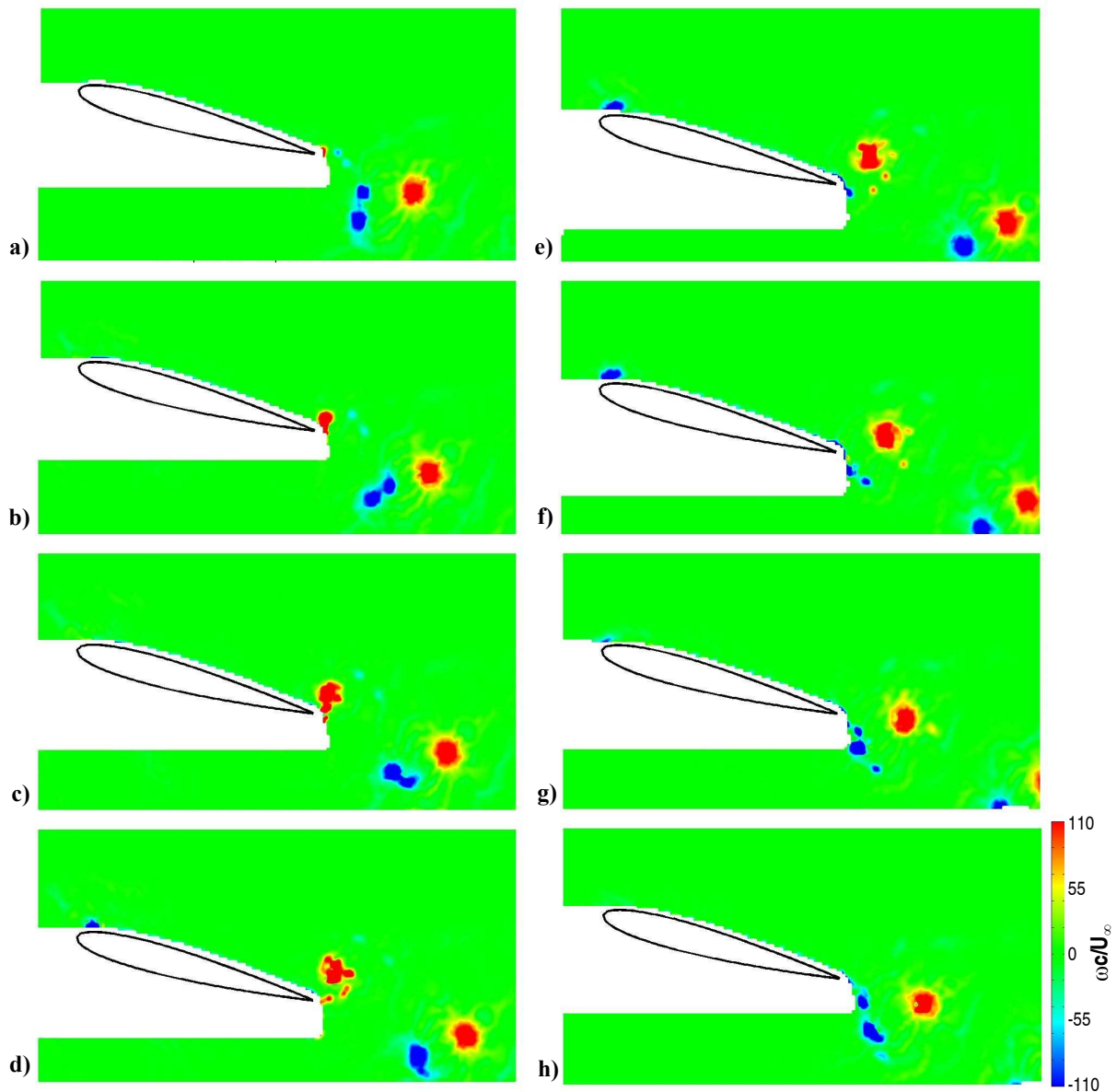
Figure 5. Phase-averaged vorticity, $\omega c/U_\infty$, throughout the cycle for $a/c = 0.050$, $Sr_c = 3.0$ demonstrating a 'mode-2' flow field. Position in the cycle denoted by diagram to left.
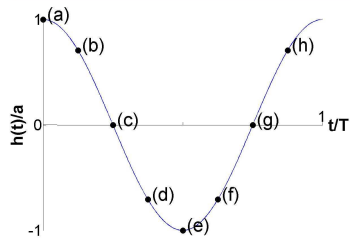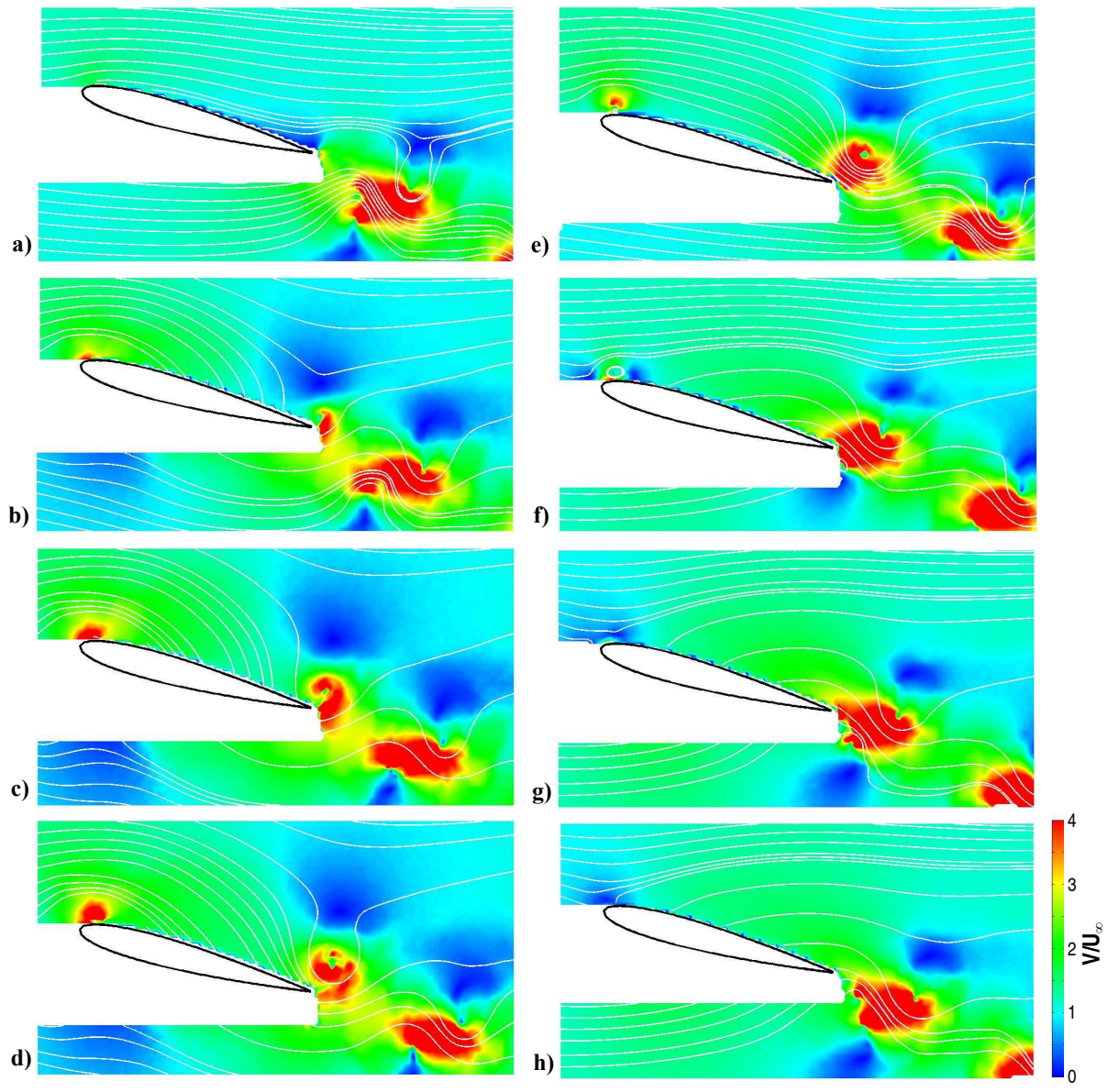
Figure 6. Magnitude of phase-averaged velocity throughout the cycle for $a/c = 0.050$ and $Sr_c = 3.0$, demonstrating a 'mode-2' flow field. Position in the cycle denoted by diagram to left.
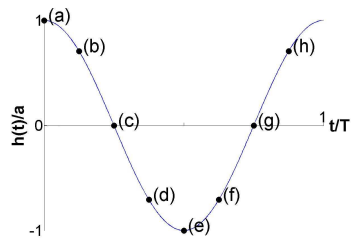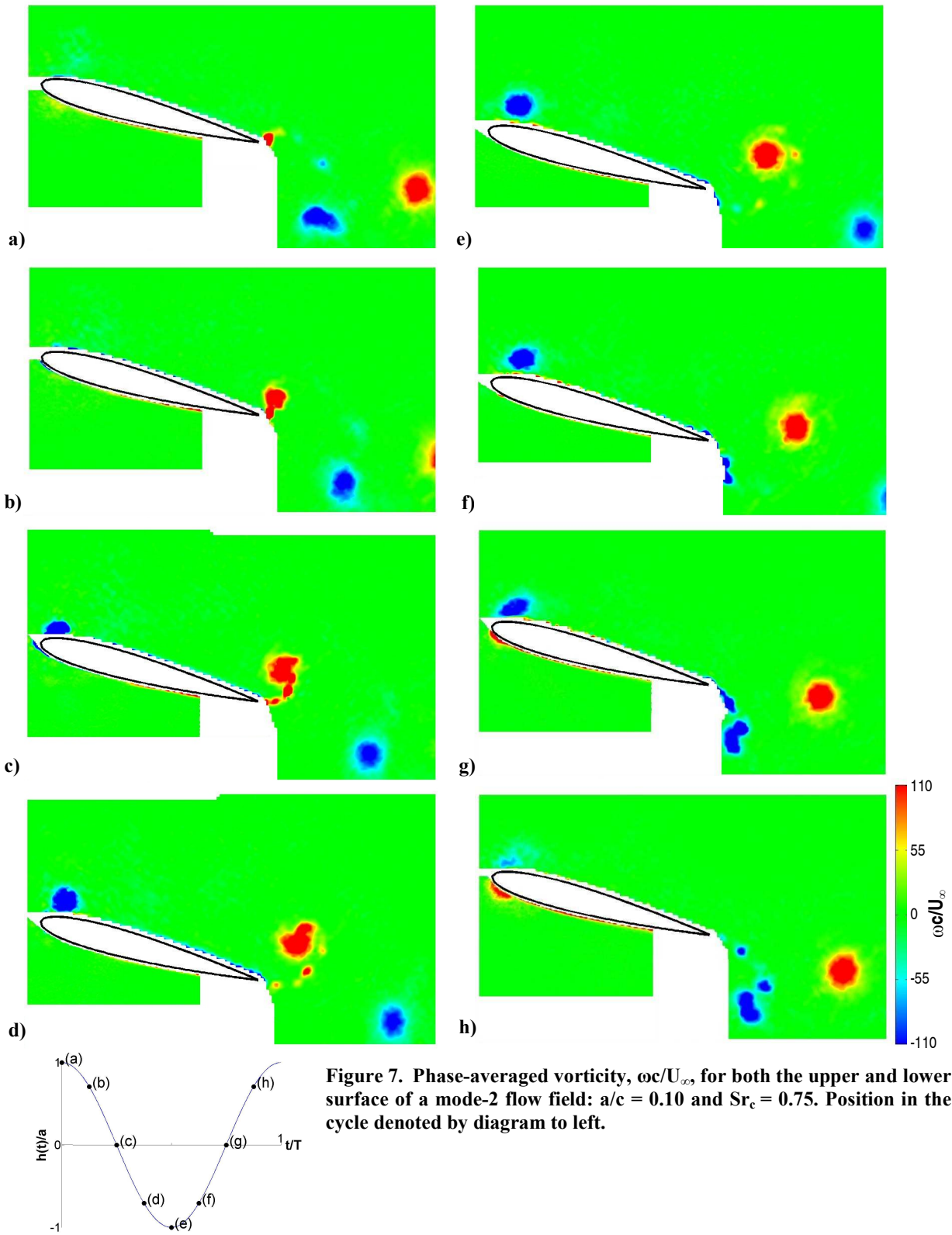
Figure 7. Phase-averaged vorticity, $\omega c/U_\infty$, for both the upper and lower surface of a mode-2 flow field: $a/c = 0.10$ and $Sr_c = 0.75$. Position in the cycle denoted by diagram to left.
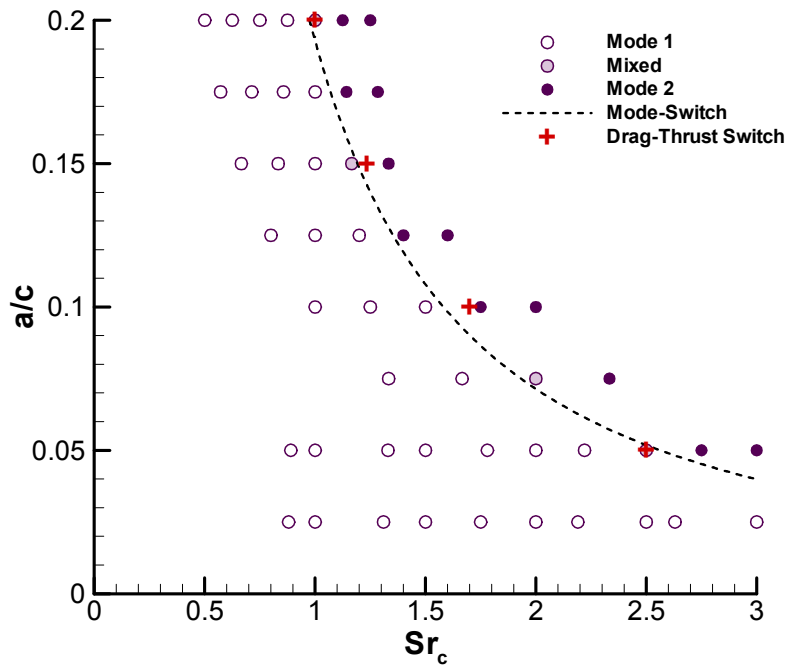
Figure 8. Mode-switch diagram derived from phase-averaged flow fields. Mode-switch dashed line is derived from power law curve fit of points for each a/c that are centrally located between the last mode-1 and first mode-2.
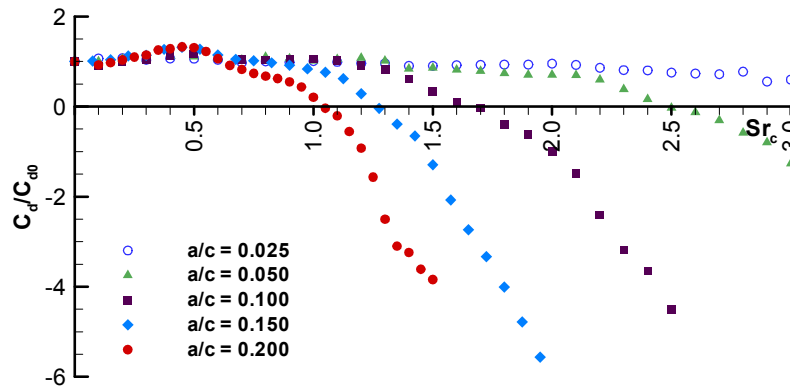

Figure 9. Normalized drag force as a function of Strouhal number based on chord length.
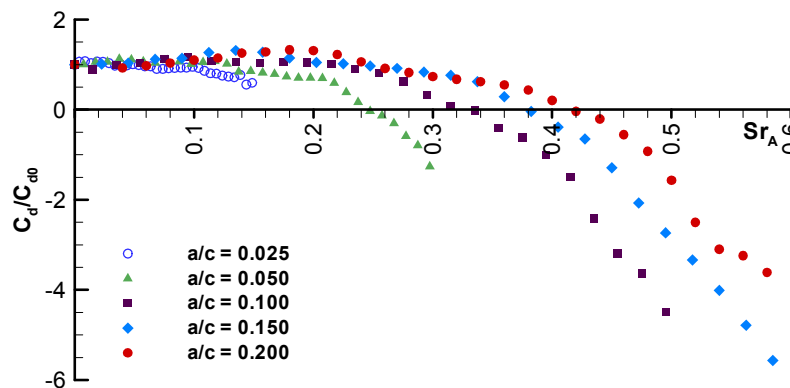

Figure 10. Normalized drag force as a function of Strouhal number based on amplitude.

American Institute of Aeronautics and Astronautics